Full Length Article

A mathematical model of osteoclast acidification during bone resorption

Frank V. Marcoline [a,b], Yoichi Ishida [c], Joseph A. Mindell [d], Smita Nayak [e], Michael Grabe [a,b,*]

[a] Cardiovascular Research Institute, University of California, San Francisco, CA 94158, USA
[b] Department of Pharmaceutical Chemistry, University of California, San Francisco, CA 94158, USA
[c] Department of Philosophy, Ohio University, Athens, OH 45701, USA
[d] Membrane Transport Biophysics Unit, National Institute of Neurological Disorders and Stroke, National Institutes of Health, Bethesda, MD 20892, USA
[e] Swedish Center for Research and Innovation, Swedish Health Services, Seattle, WA 98122, USA

ARTICLE INFO

ABSTRACT

Bone resorption by osteoclasts occurs through the creation of a sealed extracellular compartment (ECC), or pit, adjacent to the bone that is subsequently acidified through a complex biological process. The low pH of the pit dissolves the bone mineral and activates acid proteases that further break down the bone matrix. There are many ion channels, transporters, and soluble proteins involved in osteoclast mediated resorption, and in the past few years, there has been an increased understanding of the identity and properties of some key proteins such as the ClC-7 Cl^-/H^+ antiporter and the H_V1 proton channel. Here we present a detailed mathematical model of osteoclast acidification that includes the influence of many of the key regulatory proteins. The primary enzyme responsible for acidification is the vacuolar H^+-ATPase (V-ATPase), which pumps protons from the cytoplasm into the pit. Unlike the acidification of small lysosomes, the pit is so large that protons become depleted from the cytoplasm. Hence, proton buffering and production in the cytoplasm by carbonic anhydrase II (CAII) is potentially important for proper acidification. We employ an ordinary differential equations (ODE)-based model that accounts for the changes in ionic species in the cytoplasm and the resorptive pit. Additionally, our model tracks ionic flow between the cytoplasm and the extracellular solution surrounding the cell. Whenever possible, the properties of individual channels and transporters are calibrated based on electrophysiological measurements, and physical properties of the cell, such as buffering capacity, surface areas, and volumes, are estimated based on available data. Our model reproduces many of the experimental findings regarding the role of key proteins in the acidification process, and it allows us to estimate, among other things, number of active pumps, protons moved, and the influence of particular mutations implicated in disease.

1. Introduction

Bone diseases such as osteoporosis [1], osteopetrosis [2], and Paget's disease [3] are the result of an imbalance in the activity of bone-building osteoblasts and bone-resorbing osteoclasts. The most common therapies for the treatment of osteoporosis directly influence osteoclast activity, and these drugs include bisphosphonates and raloxifene. Unfortunately, these drugs only modestly reduce fracture risk [4–8], highlighting the need for new, more effective medications to help reduce osteoporosis morbidity and mortality. Most studies aimed at reducing excessive bone resorption by overactive osteoclasts have focused on changing the cell fate determination that leads to osteoclast formation or by inducing apoptosis of mature osteoclasts with bisphosphonates [1], while much less effort has been aimed at disrupting the acidic environment required for bone breakdown. The lack of research into halting acidification is due in part to the biochemical complexity, intricate geometry, and limited understanding of some of the transport proteins involved in osteoclast-mediated resorption.

Osteoclasts degrade bone through the creation of an acidic microenvironment that depends on many factors reviewed in Refs. [9,10] and summarized in Fig. 1. Osteoclasts first form a tight adhesion to the bone surface and then secret protons and proton-activated hydrolytic enzymes into the extracellular compartment (ECC) formed between the bone and the osteoclast [9]. Acidification solubilizes the bone matrix and activates acid proteases, such as cathepsins [11], which then digest the organic bone matrix [9]. Osteoclasts contain a large number of lysosomes, and the formation of the ECC occurs through lysosomal fusion with the ruffled border [12], the portion of the cell membrane that faces the resorption pit. Acidification is carried out by the bafilomycin-sensitive, vacuolar ATPase (V-ATPase) [13,14], which hydrolyzes ATP to pump protons from the cytoplasm into the ECC [15]. Mutations in the genes encoding the V-ATPase cause a rare bone disease known as osteopetrosis [2,16].
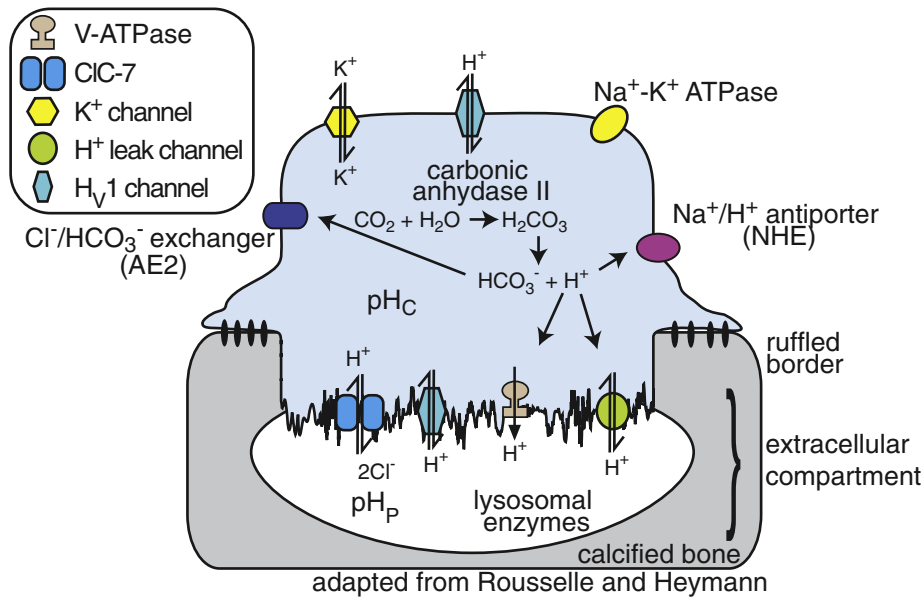
Fig. 1. Cartoon model of a resorbing osteoclast. A cartoon of an osteoclast undergoing active bone resorption including key pH regulation components (see legend). The cell forms a tight seal around the bone with the ruffled border adjacent to the bone surface. The space between the bone and the border is called the extracellular compartment (ECC) or pit. The resorbed bone is referred to as the resorption pit or the resorption lacuna. The localization of particular channels and transporters to the plasma membrane or ruffled border represented here is used throughout the manuscript, except when noted.

The V-ATPase is electrogenic [15] so that a counterion flux is needed to prevent the buildup of a large membrane potential (Ψ), which would prevent acidification. The counterion was originally thought to be carried by passive chloride channels for both acidic lysosomes [17] and osteoclasts, and mutations in the gene encoding the ClC-7 chloride channel were found to cause severe osteopetrosis in humans and mice, making chloride the prime counterion candidate and ClC-7 the probable carrier [18]. Interestingly, it was later revealed that the ClC-7 gene encodes a Cl^-/H^+ antiporter – not a channel [19]. The antiporter operates with a fixed stoichiometry that moves 2 Cl^- into the EEC for every 1 Cl^+ returned to the cytoplasm [19]. Thus, as ClC-7 operates, it reduces the membrane potential, but counterintuitively causes *alkalinization* of the extracellular pit. While the role that ClC-7 plays in acidifying lysosomes is controversial [19,20], mathematical models indicate that the antiporter facilitates greater lysosomal acidification than a simple chloride channel [21,22]. With regard to osteoclasts, deleterious mutations in ClC-7, or its β-subunit Ostm1, result in failure of the ECC to acidify [18,21,23]. Meanwhile, studies have revealed both inwardly and outwardly rectifying K^+ currents [24,25], which may also play a role in aiding acidification through neutralization of the membrane potential. The efficacy of the V-ATPase is also limited by the degree of proton leak across the membrane of acidic compartments as shown for lysosomes [26] and organelles along the secretory pathway [27]. A likely candidate for the proton leak across the ruffled border is the voltage-gated H_V1 proton channel, which is present in osteoclasts [28] and explains why Zn^{2+}, an H_V1 inhibitor, blocks cytoplasmic pH recovery after an acid load [29], and also inhibits bone resorption by isolated rat osteoclasts [30].

The most striking morphological feature of active osteoclasts are their intricate membrane folds and bristle-like surface projections that define the ruffled border [31]. These folds are thought to be important for enhancing resorption by increasing the surface-to-volume ratio of the ECC, which would allow for faster acidification of the pit by restricting its volume [32]. Also, since the ECC is large, volume restriction helps to reduce the depletion of protons in the cytoplasm. In all cellular spaces, changes in proton concentration are minimized through the intrinsic buffering capacity of the matrix as well as the buffering capacity of specific molecules such as bicarbonate. Together the enzyme carbonic anhydrase II (CAII) [33] and electroneutral Cl^--bicarbonate transporters (AE2) [34,35] prevent alkalinization of the cytoplasm during resorption through the creation of cytoplasmic protons from carbon dioxide and water, and not surprisingly mutations or disruption of either gene causes the bone disease osteopetrosis [36,37]. In addition to the role that cellular content can play in proton buffering, nonpermeant charged material, known as Donnan particles, can aid acidification through influencing the membrane potential [38].

Here we construct an ordinary differential equations (ODE)-based mathematical model of the acidification of the extracellular pit of an actively resorbing osteoclast. Since the cytoplasm is comparable in size to the ECC and the cytoplasmic proton drain is significant, we explicitly track the concentration changes of ions and relevant small molecules in both spaces, which is an advance over our previous models of organelle acidification, which ignored changes in cytoplasmic values [22,32]. The concentration changes are driven by chemical reactions specific to each space as well as fluxes across the plasma membrane and the ruffled border due to relevant channels and transporters. Proton concentration changes in the cytoplasm are influenced in the current model by Na^+/H^+ exchangers (NHE) and Cl^--bicarbonate exchangers (AE2); however, we recognize that other regulatory transporters are present such as Na^+-bicarbonate cotransport and Cl^--hydroxide (OH^-) exchangers [29,39–41]. As described in the Theory and methods and illustrated in Fig. 2, when possible we use available electrophysiological data for each transporter or channel to calibrate the single protein ionic fluxes used in the ODEs. This approach makes it possible to estimate protein copy numbers, which are very difficult to measure experimentally, while also allowing us to explore how acidification is impacted by the particular characteristics of individual proteins such as their voltage dependence and rectification properties. Additional biophysical parameters from the literature needed to construct a quantitative mathematical model have been assembled in Tables 1 and 2. We show that the model can be used to reproduce experimental acidification data, and fitting the model to the experimental data allowed us to estimate additional parameter values that could not be gleaned from the literature. Using these fitted parameters as a starting point, we carried out further tests to understand the role that individual components play in ensuring robust acidification.
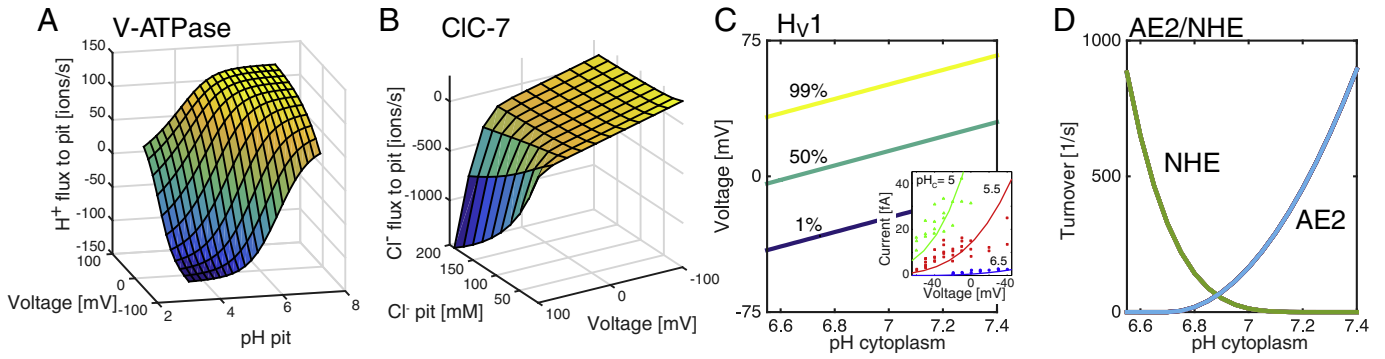
Fig. 2. Transport properties of key channels and transporters. (A) V-ATPase proton pumping rate as a function of pH_P in the ECC and membrane potential across the ruffled border (Ψ_P) based on a mechanochemical model of the transporter taken from Ref. [43]. (B) Single antiporter ClC-7 chloride flux into the pit as a function of Ψ_P and chloride concentration in the ECC as per Eqs. (2) and (3), which were developed in Ref. [22] based on experimental data. (C) H_V1 open probability as a function of membrane voltage and cytoplasmic pH_C. The inset shows single-channel currents (dots from Ref. [48]) recorded under different cytoplasmic pH values at a constant pH_E of 7.5. The solid lines are single channel currents calculated from the model in Eq. (5) with $P_{Hv1} = 1$. (D) Single transporter turnover rates for NHE (green) and AE2 (blue) based on Eqs. (6) and (7), respectively, as a function of cytoplasmic pH. AE2 is active above pH_C 7, while NHE is active below pH_C 7.

Table 1
Model Parameters.

Description	Units	Symbol	Value	Reference
Extracellular space				
Extracellular pH		pH_E	7.4	[78]
Extracellular potassium concentration	mM	$[K^+]_E$	5	[78]
Extracellular sodium concentration	mM	$[Na^+]_E$	145	[78]
Extracellular chloride concentration	mM	$[Cl^-]_E$	110	[78]
EC bicarbonate concentration	mM	$[HCO_3^-]_E$	24	a
Cytoplasmic space				
Cytosolic pH (initial)		pH_C	7.2	[79,80]
Cytosolic potassium concentration (initial)	mM	$[K^+]_C$	145	[78]
Cytosolic sodium concentration (initial)	mM	$[Na^+]_C$	10	[78]
Cytosolic chloride concentration (initial)	mM	$[Cl^-]_C$	5–50	[78,81]
Cytosolic bicarbonate concentration	mM	$[HCO_3^-]_C$	24	a
Cytosolic volume	μm^3	V_C	850	b
CO_2 hydration forward rate constant	s^{-1}	k_+	3.65×10^{-1}	[82]
CO_2 hydration reverse rate constant	$(Ms)^{-1}$	k_-	4.8×10^5	[82]
NH_3 protonation forward rate constant	$(Ms)^{-1}$	$k_{+,NH3}$	2×10^8	e
Extracellular compartment (ECC)				
ECC pH (initial)		pH_P	7.4	[78]c
ECC potassium concentration (initial)	mM	$[K^+]_P$	5	[78]c
ECC sodium concentration (initial)	mM	$[Na^+]_P$	145	[78]c
ECC chloride concentration (initial)	mM	$[Cl^-]_P$	110	[78]c
ECC volume	μm^3	V_P	100	d
Ruffled border				
Surface area	μm^2	S_P	650	d
Bilayer capacitance	$\mu F/cm^2$	C_0	1	[83]
Plasma membrane				
Surface area	μm^2	S_E	400	d
Bilayer capacitance	$\mu F/cm^2$	C_0	1	[83]
NH_3 Permeability	cm/s	P_{NH3}	4.8×10^{-2}	

a Concentration in control media used in osteoclast experiments in Ref. [84].
b Estimated from EMs assuming a spherical cap of height 5 μm and radius 15 μm [57]. See *geometry*.
c Typical extracellular values. Values in the nascent ECC are not known.
d Estimated from electron micrographs. See *geometry*.
e Arbitrary value, chosen to be the fastest reaction in the system, but slow enough for the solver to handle smoothly. The reverse rate $k_{-,NH3}$ is set by the NH_3 pK_a of 9.25.

2. Theory and methods

2.1. The mathematical model

We employ a continuum model of osteoclast driven acidification that tracks changes in two distinct compartments: the ECC and the cytoplasm, following a modeling framework established in our previous work on the acidification of organelles [22,32]. We consider the flux of molecules from the extracellular solution into the cytoplasm, but we assume that the external space is so large that concentrations are constant in time. We also assume that the ECC and cytoplasm are well-mixed environments such that spatial gradients within each compartment can be ignored. Future studies will rigorously probe the validity of this later assumption. In what follows, time-dependent variables track the number of particles, while variables in square brackets denote molar concentrations. Quantities with the subscript C are cytoplasmic, P are in the pit and E are extracellular. Flux values corresponding to chemical reactions and transport/channel mediated changes are provided in units of ions per second. We assume that exchange occurs between the ECC and cytoplasm and the extracellular solution and cytoplasm, but not directly between the extracellular solution and the ECC. Membrane proteins are localized to specific membranes, either the plasma membrane or the ruffled border, endowing each membrane with particular transport properties. Next, we describe the individual components that make up the model.

2.2. Membrane potential

We adopt a physical model of the membrane potential that follows the work of Rybak and co-workers [42] and depends on the net difference in accumulated charge within a given compartment:

$$\Psi = \frac{FV}{C_0 S}\left(\sum[\text{cations}] - \sum[\text{anions}] - \sum[\text{impermeant ions}]\right), \quad (1)$$

where C_0 is the membrane capacitance per unit area, F is Faraday's constant, and S and V are the surface area and volume of the cellular compartment, respectively. Given simplified geometry in Fig. 1, we assume that the potential across the ruffled border (Ψ_P) is the sum of all ionic charge in the pit, while the membrane potential across the plasma membrane (Ψ_E) is the charge imbalance of the contents in the cytoplasm and pit. The concentration of impermeant anions (D), known as Donnan particles, reflects the fact that there is often negatively charged protein and polymer in cellular environments that influences the distribution of permeant ions. We have adopted the standard convention in which positive membrane potential values indicate an excess of positive

Table 2
System parameters determined from optimization.

Description	Units	Symbol	Figure 3	Figure 4a	Figure 4b	Figure 5 & 6	Figure 6	Figure 6
						ClC–7 only	Channel only	Mixed
Plasma membrane/Cytoplasm								
Potassium permeability	cm/s	P_K	4.0×10^{-7}	4.0×10^{-7}	4.0×10^{-7}	4.0×10^{-7}	4.0×10^{-7}	4.0×10^{-7}
Chloride permeability	cm/s	P_{Cl}	5.8×10^{-8}	5.8×10^{-8}	5.8×10^{-8}	5.8×10^{-8}	5.8×10^{-8}	5.8×10^{-8}
Number of H$_V$1 proton channels		N_{Hv1}	218,922	218,922	226,478	226,478	226,478	226,478
Number of AE2 Cl$^-$/HCO$_3^-$ exchangers		N_{AE}	337,974	337,974	337,974	337,974	337,974	337,974
Number of NHE Na$^+$/H$^+$ exchangers		N_{NHE}	212,941	213,218	213,218	213,218	213,218	213,218
Na$^+$/K$^+$–ATPase whole cell Na$^+$ efflux	mM/min	$3{\cdot}F_{NaK}$	12.2	0	0	10.0	9.3	9.5
Carbon dioxide concentration	mM	$[CO_2]_C$	1.2	7.4×10^{-4}	7.4×10^{-4}	1.77	1.77	1.77
Initial bicarbonate concentration	mM	$[HCO_3^-]_C$	24	1.0×10^{-2}	1.0×10^{-2}	24.0	24.0	24.0
Ruffled border/ECC								
Passive proton permeability	cm/s	P_H				8.8×10^{-6}	8.8×10^{-6}	8.8×10^{-6}
Chloride permeability	cm/s	P_{Cl}				0	1.5×10^{-6}	7.6×10^{-8} [a]
Number of V-ATPase proton pumps		N_V				528,286	355,865	552,344
Number of ClC–7 Cl$^-$/H$^+$ antiporters		N_{ClC}				200,490	0	120,294 [b]
Other								
Acid load (initial [NH$_3$]$_C$+[NH$_4^+$]$_C$)	mM	N/V_C		29.5	36.7			
Bath NH$_3$ removal rate constant	s	τ		4.9	3.1			

Greenshaded boxes were determined from fitting procedure.

[a] 5% of P_{Cl^-} from Cl$^-$ channel only simulation.

[b] 60% of N_{ClC} from ClC–7 only simulation.

charge in the cytoplasm relative to the extracellular medium or the pit. We ignore charge accumulation along the surface of the bone, which would increase the capacitance of the pit, and we also ignore the influence that convoluted and stacked membrane folds in the ruffled border may have on decreasing the capacitance of the ruffled border.

2.3. V-ATPase proton pump

The ATP dependent flux of protons through a single V-ATPase is given by J_V(pH$_C$, pH$_P$, Ψ_P) which has been determined from a detailed mechanochemical model calibrated against experimental current-voltage data [43]. A high-resolution structure of a eukaryotic V-ATPase from *Saccharomyces cerevsiae* was recently determined revealing for the first time that this family member has 10 copies of the proton carrying C-subunit [44]. Thus, each revolution of the rotor domain consumes 3 ATP molecules and transports 10 H$^+$ across the membrane placing bounds on the proton motive force that the V-ATPase can achieve [44]. Our mechanochemical model used to determine J_V is described in Grabe and Oster [32] with the following slight modifications: a 10 H$^+$:3 ATP stoichiometry, an increase in the rotor domain radius to 40 Å, and a buried pK$_a$ value for the titratable site of 8.4. This flux depends on the membrane potential across the ruffled border Ψ_P, the pH of the pit, and the cytoplasmic pH, which we assume can change during acidification. We do not have a closed analytic form for this term, but rather we use a pre-computed single-pump performance surface as shown in Fig. 2A. The total V-ATPase dependent proton movement is given by multiplying the single-pump flux by the number of V-ATPases, N_V. We assume that V-ATPases only localize to the ruffled border.

2.4. ClC-7 chloride-proton antiport

ClC-7 antiporters are assumed to localize to the ruffled border where they exchange two Cl$^-$ for a single H$^+$. Previously, we calibrated the single antiporter turnover rate against electrophysiological recordings, providing the following analytic expression [22], which depends on the pH gradient across the ruffled border, the ruffled border membrane potential, and the chloride concentrations in the cytoplasm and the pit:

$$J_{ClC} = x \times a\Delta p_{ClC} + (1-x) \times b(\Delta p_{ClC})^3, \tag{2}$$

where a is 0.3, b is 1.5×10^{-5}, Δp_{ClC} is the driving force for ClC-7 turnover:

$$\Delta p_{ClC} = 3\Psi_P + \frac{k_B T}{e}\left(2.3\Delta pH + 2\ln\left(\frac{[Cl^-]_C}{[Cl^-]_P}\right)\right), \tag{3}$$

and x is a simple switching function equal to $(1/2 + 1/2\tanh((\Delta p_{ClC} + 250)/75))$. In addition to matching macroscopic experimental data, Eq. (3) obeys detailed balance, and the maximum turnover rate was estimated based on single protein rates obtained from a bacterial homologue [45]. This simple model (Eqs. (2) and (3)) does not account for saturation of the transport rate under large driving forces, but it does faithfully fit experimental data between −150 mV and +100 mV under typical chloride concentrations near neutral pH [22]. The single antiporter pumping performance surface is pictured in Fig. 2B. The total ClC-7 dependent pumping rate is given by the number of active ClC-7 antiporters, N_{ClC}, times the single turnover rate, times 2 for chloride and 1 for protons.

2.5. Cl$^-$, K$^+$, and H$^+$ leak channels

We model passive channels with the following generic form:

$$J_X = P_X S \frac{qU\left([X]_i - [X]_j e^{qU}\right)}{1-e^{qU}}, \tag{4}$$

where q is −1 for monovalent anions and +1 for monovalent cations, S is the membrane surface area, U is the reduced membrane potential (U = $e\Psi/k_B T$), and [X] is the concentration of ion X on side i or j of the membrane. In the presence of chloride and potassium channels, we set the permeability coefficient, P_X, to a large value 10^{-6} to 10^{-8} cm/s allowing these ions to quickly equilibrate across the membrane, and for simulations in which we assume no counterion channels, we set the permeability coefficients to zero. We always have K$^+$ and Cl$^-$ channels on the plasma membrane, and we will explore scenarios in which K$^+$, Cl$^-$ and H$^+$ channels are sometimes on the ruffled border.

2.6. Voltage-gated proton channels

Voltage-gated proton currents that are inhibited by zinc have been measured in osteoclasts [28,29], and here, we adapt a mathematical

model of the H_V1 family member [46,47] developed based on single-channel currents measured by DeCoursey and co-workers [48]. We assume that these channels localize to both the ruffled border and the plasma membrane. Our model is similar to the simple chloride and potassium channel model in Eq. (4), but we incorporate a prefactor, P_{Hv1}, that accounts for channel gating by pH_P, pH_C, pH_E, and membrane potential as well as terms needed to match experiments:

$$J_{Hv1} = \sigma_{Hv1} \cdot P_{Hv1} \cdot pH_{P/E} \cdot |\Delta p_H| \frac{U\left([H^+]_{P/E} - [H^+]_C e^{+U_{P/E}}\right)}{1 - e^{+U_{P/E}}}$$

$$P_{Hv1}\left(pH_C, pH_{P/E}, \Psi_{P/E}\right) = \frac{1}{1 + e^{-(\Psi_{P/E} - V_{1/2})/k}} \tag{5}$$

$$V_{1/2} = -40 \cdot \left(pH_{P/E} - pH_C\right) + 30 \text{ mV},$$

where σ_{Hv1} is a scaling factor, k is 8 mV and controls the voltage-dependence of opening, $V_{1/2}$ is the voltage threshold for channel opening, which is pH dependent, and Δp_H is the proton motive force (PMF) across the membrane:

$$\Delta p_H = \Psi_{P/E} - \frac{k_B T}{e} \ln\left(\frac{[H^+]_C}{[H^+]_{P/E}}\right).$$

The prefactor σ_{Hv1} was determined by fitting the model to single channel data [48] shown in the inset of Fig. 2C using the fminsearch function in Matlab™, while simultaneously fitting the macroscopic currents from Ref. [49] with an additional parameter corresponding to the total number of channels in the cell (not shown). Only σ_{Hv1} and the total channel number were free parameters, while k and the constant terms in Eq. (5) for $V_{1/2}$ were taken from experiment [48]. Phenomenologically, we write the proton current as a function of $pH_{P/E}$ and Δp_H since these terms are required to fit the macroscopic currents, where the subscripts P and E depend on where the channel is localized. As with the other channels and transporters in this study, we have ignored the gating dynamics, which have been modeled elsewhere [50], because we assume that pit acidification occurs on a long timescale compared to channel gating, and channels adopt their steady state open probability. Moreover, state-dependent kinetic models of channel opening have also been constructed that nicely fit currents and fluorescent data reporting on conformational changes in the protein [51]. The total proton flux across the ruffled border or plasma membrane is given by the number of active channels, N_{Hv1}, in the respective membrane multiplied by the single channel flux, J_{Hv1}.

2.7. Na^+/H^+ exchangers

Non-resorbing osteoclasts employ Na^+/H^+ exchangers (NHE) in the plasma membrane to control cytoplasmic pH levels, and the NHE1 isoform is expressed in avian osteoclasts [52]. During an internal acid load, cells extrude excess protons via the exchanger to restore basal pH levels [29,41]. Here we adopt a simple model for the action of a single NHE exchanger loosely adapted from the work of Leem and co-workers [41]:

$$J_{NHE} = P_{NHE}^2(pH_C)V_{NHE}\frac{\Delta\mu_{NHE}}{K_{NHE} + |\Delta\mu_{NHE}|},$$

where

$$\Delta\mu_{NHE} = k_B T \ln\left(\frac{[H^+]_E[Na^+]_C}{[H^+]_C[Na^+]_E}\right),$$

and

$$P_{NHE}(pH_C) = \begin{cases} 1 & pH_C < 6.55, \\ (7.25 - pH_C)/0.7 & 6.55 \le pH_C < 7.25, \\ 0 & pH_C \ge 7.25. \end{cases} \tag{6}$$

We assume that NHE localizes only to the plasma membrane where it aids in stabilizing the cytoplasmic pH. The flux is expressed as a function of the chemical potential, $\Delta\mu_{NHE}$, to enforce detailed balance at equilibrium, and an open probability, P^2_{NHE}, is employed to account for the cytoplasmic pH dependence of activity. Squaring P_{NHE} smooths the function at the transition regions. The maximum single exchanger turnover, V_{NHE}, is set to 1454 s^{-1}, which is estimated from rates for the bacteria transporter NhaA [53], K_{NHE} is 3 $k_B T$, which was based, in part, on attempts to match Eq. (6) to the whole cell flux in Ref. [41] and the model to the data in Fig. 4. The NHE flux as a function of pH_C is shown in Fig. 2D. K_D values are typically expressed in units of concentration; however, here we express the flux as a function of the driving force, which is why K_{NHE} has units of energy. The general shape of the single transporter dependent turnover as a function of pH_C (Fig. 2D) is similar to whole cell fluxes recorded from ventricular myocytes [41] suggesting that Eq. (6) is a reasonable approximation of NHE transport. At pH_C 6.55, below which experimental currents were not measured, the flux exhibits a kink from enforcing transporter saturation at low pH. In the calculations presented here, pH_C never reaches this low value, but we caution users of our code when exploring scenarios with acidic cytoplasmic values. The total flux due to NHE transporters is the copy number, N_{NHE}, times J_{NHE}.

2.8. Cl^-/HCO_3^- exchanger

Chloride-bicarbonate exchangers (AE2) trade Cl^- for HCO_3^- across the plasma membrane with a 1-to-1 stoichiometry. AE2 knockouts in mice result in severe osteopetrosis, and immunohistochemistry reveals that the transporter is exclusively localized to the plasma membrane [37]. The transporter is not electrogenic, and therefore lacks voltage dependence, but it has been shown to have a dependence on extracellular and cytoplasmic pH values [54]. We model the single exchanger transporter rate with a similar form to the NHE transporter:

$$J_{AE} = P_{AE}^2(pH_C)V_{AE}\frac{\Delta\mu_{AE}}{K_{AE} + |\Delta\mu_{AE}|},$$

where

$$\Delta\mu_{AE} = k_B T \ln\left(\frac{[HCO_3^-]_E[Cl^-]_C}{[HCO_3^-]_C[Cl^-]_E}\right),$$

and

$$P_{AE}(pH_C) = \begin{cases} 0 & pH_C < 6.7, \\ (pH_C - 6.7)/0.75 & 6.7 \le pH_C < 7.45, \\ 1 & pH_C \ge 7.45. \end{cases} \tag{7}$$

Here, $K_{AE} = 1.7 k_B T$, and the pH_C dependence of the prefactor P_{AE} is based on AE fluxes measured in ventricular myoctes [41]. The value of K_{AE} is determined based on the observation that the apparent K_m for external Cl^- is 5.6 mM [54]. Under normal operating conditions in our model, AE2 imports Cl^- as it exports bicarbonate, and the chemical potential, $\Delta\mu_{AE}$, is dominated by the external chloride so we set $K_{AE} = |\Delta\mu_{AE}| = |k_B T \ln((24\cdot50)/(24\cdot110))| = 0.8 k_B T \sim 1 k_B T$, where we substituted typical cytoplasmic concentration values, 24 mM nominal external bicarbonate, and 110 mM external Cl^-. Again, K_{AE} has units of energy since the flux is a function of chemical potential. Maximum transporter turnover rates are difficult to obtain, and for convenience, we set V_{AE} to $V_{NHE} = 1454$ s^{-1}. We ignore the dependence on

extracellular pH since it is constant in the current model. As with the NHE model, P_{AE} exhibits a kink at pH_C 7.45. Our model never reaches such high pH values, but caution should be taken when using our code to explore alkaline cytoplasmic pH values. The total flux to AE2 is given by J_{AE} times the total number of active exchangers, N_{AE}.

2.9. Na$^+$/K$^+$-ATPase

Osteoclasts have been shown to have a high number of plasma membrane Na$^+$/K$^+$-ATPases on the order of 5 million [55], similar to other cell types such as HeLa cells, which have been estimated to express millions of Na$^+$/K$^+$-ATPases [56]. Here we assume that Na$^+$/K$^+$-ATPase dependent transport of Na$^+$ and K$^+$ across the plasma membrane is constant in time with a whole-cell transport rate of F_{NaK}. Each cycle expels 3 Na$^+$ and imports 2 K$^+$, leading to a rate of change of -3 F_{NaK} and $+2$ F_{NaK}, respectively.

2.10. Geometry

The size of the ECC is defined in part by the annular ring of actin, known as the sealing zone, that tightly adheres the ruffled border to the bone surface to seal off the pit. Based on confocal images of F-actin staining, this area is about 200 µm^2 for actively resorbing rabbit osteoclasts [57], which forms a lower bound on the surface area of the ruffled border if the membrane is stretched tightly across the zone. We realize that the actual membrane area is higher due to its folds, and our base simulations will employ a ruffled border surface area, S_P, of 650 µm^2. Based on electron micrographs (EMs) the distance from the ruffled border to the bone surface appears to be 0.2–1 µm [31,58], providing an initial estimate of the ECC volume, V_P, between 40 and 200 µm^3. Here we start with a base value of 100 µm^3. The volume and surface area of the osteoclast were also estimated from the same confocal images [57]. The cells are rounded, similar to the "rounded and compact" phenotype associated with active bone resorption [59], with a height of 5 µm and a radius of ~10 µm [57]. The latter value is consistent with a 14 µm radius reported by Nordström and co-workers [29]. Using the spherical cap formula and excluding the ruffled border base, we arrive at an extracellular-to-plasma membrane surface area, S_E, of ~400 µm^2 and a total cytoplasmic volume of 850 µm^3. Since it is estimated that 35% of the cell is occupied by organelles [60], the cytoplasmic volume of distribution, V_C, in the cap would be smaller, but we also realize that V_C extends below the cap into the pit. Thus, we start by assuming V_C is 850 µm^3. Since these values are far from precise, and true volumes and surface areas vary from cell-to-cell, we will explore a wide range of surface areas and volumes to determine their influence on the steady state and dynamic properties of resorption.

2.11. Intrinsic and specific buffering mechanisms

Changes in the free proton concentration are tightly regulated by the buffering capacity of the intracellular and extracellular spaces. Mathematically, this relationship can be represented as $\Delta pH = -\Delta[H^+]/\beta$, where β is the buffering capacity of the medium. The total buffering power of a space is the sum of its individual components. We assume that there is an intrinsic buffering capacity (β_i) corresponding to the net action of titrating all of the resident proteins and molecules as well as a specific buffering capacity (β_1) due to bicarbonate (HCO$_3^-$), the primary molecule used to buffer the cytoplasmic pH. Rather than tracking the buffered protons *implicitly* through a buffer term, we track the protons *explicitly* through a series of acid-base reactions that take place in the cytoplasm or in the ECC. Each reaction takes the form:

$$B_i^- + H^+ \leftrightarrow HB_i, \tag{8}$$
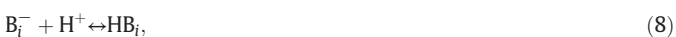
resulting in a differential equation of the form:

$$\frac{d}{dt}B_{i,P}^- = N_A V_P \left(k_-^{B_{i,P}}[HB_i]_P - k_+^{B_{i,P}}[B_i^-]_P[H^+]_P \right), \tag{9}$$

for species i in the pit (P). For the cytoplasm, we employ a single buffer species of 47 mM with a pK$_a$ of 6.34 resulting in a buffering capacity of 20–25 mM/pH between pH$_C$ 5.5 and 7 as employed by Ravesloot and co-workers based on their measurements carried out on osteoclasts derived from rat [40]. The buffering capacity of a single species with fixed concentration is given by:

$$\beta(pH) = \frac{2.3 \, B \, 10^{-pK_a} \cdot 10^{-pH}}{\left(10^{-pK_a} + 10^{-pH}\right)^2},$$

where B is the concentration of the buffer molecule.

Since the pit experiences a much wider range of pH values, we use 10 buffer species of 15.3 mM each with evenly spaced pK$_a$ values from 2.0 to 8.9. The composite total intrinsic buffering capacity is very flat between pH$_P$ 2 and 8 with a value of 25 mM/pH unit. Thus, we assume that the ECC has a constant intrinsic buffering capacity similar to lysosomes with a value of 25 mM/pH, within the range of values reported in the literature [20,26]. Protonation reactions in solution are quite fast, and we set the forward rates (k_+) in Eq. (9) to 10^8 s^{-1}, while the deprotonation rates (k_-) are set by the pK$_a$ of the buffer, $k_- = k_+ \cdot 10^{-pK_a}$. We note that water is one of these buffer molecules, but its buffering capacity is only substantial below pH 2 or above pH 13, which is outside of the pit and cytoplasm pH values calculated here. Thus, we do not include water as a buffer molecule.

For the bicarbonate, the reversible acid-base reaction is:

$$CO_2 + H_2O \underset{k_-}{\overset{k_+}{\rightleftarrows}} H_2CO_3 \leftrightarrow H^+ + HCO_3^-, \tag{10}$$
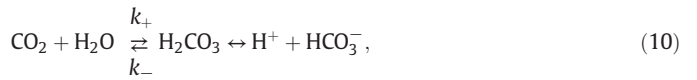
which is catalysed by the enzyme carbonic anhydrase II (CAII). As the cytoplasm is depleted of protons during active resorption, the acid-base equilibrium is maintained through the creation of additional H$^+$ and bicarbonate from carbonic acid (H$_2$CO$_3$). Since CO$_2$ freely diffuses across cellular membranes, the total carbonic acid is essentially constant, and it can be shown that the buffering capacity is proportional to the total bicarbonate [61]:

$$\beta_1 = 2.3 \cdot [HCO_3^-]_C. \tag{11}$$

The time dependent change in the bicarbonate concentration follows from Eq. (10) and takes a similar form to Eq. (9). Please see Table 1 for additional parameters. Thus, the total buffering capacity of the cytoplasm is

$$\beta_T = \beta_i + \beta_1.$$

2.12. Modeling acid load

To simulate acid loading in Fig. 4 by addition of NH$_4$Cl to the bath, we load the cytoplasm with an equilibrated quantity of NH$_3$ and NH$_4^+$, assuming a pK$_a$ of 9.25. The initial external NH$_3$ concentration is set equal to the initial cytoplasmic NH$_3$ concentration. To model bath exchange at time t_0 to a NH$_3$ free solution, we remove the external ammonia exponentially according to the following equation:

$$[NH_3]_E(t) = [NH_3]_E(t_0)e^{-(t-t_0)/\tau}, \tag{12}$$

while also modeling the passive flux of neutral NH$_3$ across the plasma membrane using Eq. (4) with a large permeability coefficient of 4.8 ×

10^{-2} cm/s. NH_3 rapidly diffuses out of the cytoplasm due to the concentration gradient, driving NH_4^+ dissociation causing a sudden pH_C drop.

2.13. Numerical solutions

The full system of equations for this model is:

$$\frac{d}{dt}H_P^+ = N_V J_V - N_{ClC} J_{ClC} - N_{Hv1} J_{Hv1} - P_H S_P J_H$$
$$+ N_A V_P \sum_{i=1}^{n_P} \left(k_-^{B_{i,P}} [HB_i]_P - k_+^{B_{i,P}} [B_i^-]_P [H^+]_P \right)$$

$$\frac{d}{dt}Cl_P^- = 2N_{ClC} J_{ClC} - P_{Cl} S_P J_{Cl}$$

$$\frac{d}{dt}B_{i,P}^- = N_A V_P \left(k_-^{B_{i,P}} [HB_i]_P - k_+^{B_{i,P}} [B_i^-]_P [H^+]_P \right) \text{ for } 1 \leq i \leq n_P$$

$$\frac{d}{dt}D_P^- = 0$$

$$\frac{d}{dt}H_C^+ = -\frac{d}{dt}H_P^+ - N_{NHE} J_{NHE} + N_{Hv1}^E J_{Hv1}^E + N_A V_C (k_+ [CO_2]_C - k_- [HCO_3^-]_C [H^+]_C)$$
$$+ N_A V_C \left(k_-^{NH_3} [NH_4^+]_C - k_+^{NH_3} [NH_3]_C [H^+]_C \right)$$
$$+ N_A V_C \sum_{i=1}^{n_C} \left(k_-^{B_{i,c}} [HB_i]_C - k_+^{B_{i,c}} [B_i^-]_C [H^+]_C \right)$$

$$\frac{d}{dt}Cl_C^- = -\frac{d}{dt}Cl_P^- + P_{Cl}^E S_C J_{Cl}^E - N_{AE} J_{AE}$$

$$\frac{d}{dt}K_C^+ = -\frac{d}{dt}K_P^+ + P_K^E S_C J_K^E + 2F_{NaK}$$

$$\frac{d}{dt}Na_C^+ = N_{NHE} J_{NHE} - 3F_{NaK}$$

$$\frac{d}{dt}NH_{4\,C}^+ = N_A V_C \left(k_+^{NH_3} [NH_3]_C [H^+]_C - k_-^{NH_3} [NH_4^+]_C \right)$$

$$\frac{d}{dt}NH_{3\,C} = P_{NH_3}^E S_C J_{NH_3} - N_A V_C \left(k_+^{NH_3} [NH_3]_C [H^+]_C - k_-^{NH_3} [NH_4^+]_C \right)$$

$$\frac{d}{dt}HCO_{3\,C}^- = N_{AE} J_{AE} + N_A V_C (k_+ [CO_2]_C - k_- [HCO_3^-]_C [H^+]_C)$$

$$\frac{d}{dt}B_{i,C}^- = N_A V_C \sum_{i=1}^{n_C} \left(k_-^{B_{i,c}} [HB_i]_C - k_+^{B_{i,c}} [B_i^-]_C [H^+]_C \right) \text{ for } 1 \leq i \leq n_C$$

$$\frac{d}{dt}D_C^- = 0$$

$$\Psi_P = -\frac{e}{C_0 S_P} \left(H_P^+ - Cl_P^- + K_P^+ - D_P^- - \sum_{i=1}^{n_P} B_{i,P}^- \right)$$

$$\Psi_E = \frac{e}{C_0 S_P} \left\{ \left(H_P^+ - Cl_P^- + K_P^+ - D_P^- - \sum_{i=1}^{n_P} B_{i,P}^- \right) + \left(H_C^+ - Cl_C^- + K_C^+ \right. \right.$$
$$\left. \left. + Na_C^+ - HCO_{3\,C}^- + NH_{4\,C}^+ - D_C^- - \sum_{i=1}^{n_c} B_{i,C}^- \right) \right\}$$

The equations were solved in Matlab™ with the ODE15s variable time step, stiff solver. The absolute and relative tolerances were set to 10^{-6}, and all calculations presented here were checked to ensure proper convergence. The initial time step size (set automatically by initial rates), minimum step size (10^{-13}), and maximum step size (10% of total time span) were all ODE15s default values.

2.14. Fitting data

We employed the Nelder-Mead search algorithm as implemented in Numerical Recipes to fit the mathematical model to the experimental data [62]. While there are many unknown parameters in our model, we chose to fit the data by optimizing the number of membrane transport proteins on the ruffled border ($P_{Cl}, P_H, N_V, N_{Hv1}, N_{ClC}$), plasma membrane transport related variables ($P_{Cl}, P_K, N_{NHE}, N_{AE}, J_{NaK}$), and cytoplasmic CO_2 and initial HCO_3^- levels (see Table 2). Only a subset of these parameters are varied in any given fit. The acidification data from Silver and co-workers [63], Nordstrom and co-workers [29], and Teti and co-workers [35] were manually digitized with Plot Digitizer (*J. A. Huwaldt and S. Steinhorst, Plot Digitizer 2.6.6, 2014, http://plotdigitizer.sourceforge.net/*), and the goodness of each fit was scored as the sum of the squared difference between the digitized pH value and the corresponding model pH value at a given point in time.

3. Results

We first use the model to explore cellular mechanisms of cytoplasmic pH regulation in response to changes in the external environment. By fitting the model to published data, we are able to estimate free parameters such as the number of pumps and channels, but more importantly, we will test whether the model correctly responds to experimental perturbations. Next, we simulate acidification of the pit and attempt to match numerical results with measurements on cultured osteoclasts. Finally, we use the parameterized model to address outstanding questions regarding the importance of particular transporters, enzymes and system geometry.

3.1. Regulation of cytoplasmic pH

Cytoplasmic pH regulation is crucial to normal cellular homeostasis, and it is particularly important to active osteoclasts, which are prone to alkalinization due to the extrusion of large quantities of protons into the extracellular pit. Typical cytoplasmic pH values are around 7.2, and different classes of transporters are employed for increasing versus decreasing the pH. The AE2 transporter is one of the primary membrane proteins responsible for protecting against alkalinization. As cytoplasmic pH increases, AE2 becomes more active resulting in bicarbonate export and Cl^- import with a 1-to-1 stoichiometry. The removal of HCO_3^- pushes the acid-base equilibrium to the right in Eq. (8) resulting in the creation of free protons. Schlesinger and colleagues explored the role of chloride-bicarbonate exchange in regulating cytoplasmic pH through a series of experiments carried out on avian osteoclasts. They concluded that the transporter enables cells to maintain normal pH levels even in the face of a large proton efflux and that acidification is absolutely dependent on external chloride [35].

We used the model to reproduce the cytoplasmic pH changes induced by extracellular chloride removal in the Schlesinger experiments (Fig. 3A). Cells were prepared on glass chips containing 110 mM Cl^- in the external buffer with 25 mM HCO_3^-, loaded with a pH indicator, and allowed to equilibrate to a pH_C near 6.9 in a nominally bicarbonate free buffer (open circles from Ref. [35]). The cells were then moved at 32 min to an isoosmotically-balanced solution free of external Cl^- (first arrow), and pH_C increased to 7.4. At 58 min (second arrow), the cells were moved back to a Cl^- containing solution, and rapid re-acidification followed. We solved the model using the standard parameters listed in Table 1 for a non-resorbing osteoclast. That is, we assumed that there was no active transport across the ruffled border and all values in Table 1 corresponding to the ruffled border were set to zero (see figure captions for any parameters that differ from table values). To mimic the experimental conditions, the external chloride solution was changed from 110 mM to 5 mM at 32 min and then it was returned to 110 mM at 58 min. The external bicarbonate concentration was not reported, and we assume a value of 3 mM throughout the timecourse.
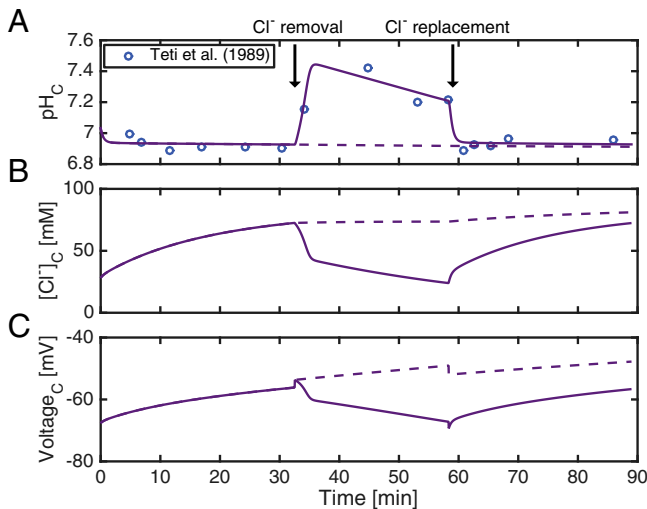
Fig. 3. Cytoplasmic pH depends on external chloride. (A) The cytoplasmic pH of avian osteoclasts responds to changes in extracellular Cl⁻ concentrations (blue circles from Ref. [35]). Experimentally, the external solution was nominally HCO₃⁻ free (modeled as 3 mM) and 110 mM [Cl⁻]$_E$. At 32 min (first arrow), cells are transferred to Cl⁻ free solutions (modeled as 5 mM), and the cytoplasm alkalinizes. At 58 min (second arrow), cells are returned to 110 mM [Cl⁻]$_E$, and pH$_C$ returns to baseline. The model was fit to the data using N_{AE}, passive chloride permeability across the plasma membrane (P_{Cl}), and the Na⁺/K⁺-ATPase whole cell current as fitting parameters with external chloride changes at both arrows resulting in 337,974 AE2 transporters and P_{Cl} as 5.8×10^{-8} cm/s (purple curve). Calculations were repeated holding the chloride and bicarbonate flux mediated by AE2 constant throughout the chloride removal phase (dashed purple curve) indicating that the pH$_C$ changes in our model are mediated primarily by the AE2 anion exchanger. (B) Cytoplasmic chloride concentrations and (C) membrane potential across the plasma membrane corresponding to the calculations in panel A (colour scheme same as panel A).

Next, we carried out a parameter search on N_{AE}, plasma membrane P_{Cl}, and Na⁺/K⁺-ATPase whole cell flux in an attempt to best match the experimental data as explained in the *Theory and methods*. The final values corresponding to the results in Fig. 3 are listed in Table 2.

At time zero, pH$_C$ slightly acidifies from 7.0 to 6.9 (Fig. 3A), as observed experimentally, due to efflux of cytoplasmic HCO₃⁻ buffer via AE2 in response to the low extracellular bicarbonate (3 mM compared to typical blood plasma levels of 24 mM). When external Cl⁻ is reduced at 32 min, the model shows a very fast increase in pH to just over 7.4. Alkalinization occurs because the driving force for AE2 is perturbed leading to Cl⁻ efflux and HCO₃⁻ entry, despite nominal 3 mM HCO₃⁻ in solution. As bicarbonate enters the cell, H⁺ buffering raises the pH. Restoring the external Cl⁻ at 58 min again switches the direction of AE2 transport causing a removal of cytoplasmic HCO₃⁻ and a return to pH$_C$ ~ 6.9. The amplitude and rate of alkalinization depends on several factors including the number of AE2, the chloride permeability, and the amount of external bicarbonate as well as other factors. The optimal fit in Fig. 3 results in 337,974 AE2 transporters, which is our best estimate for copy number of this protein on the plasma membrane of osteoclasts.

We redid the calculations holding the AE2 flux constant during chloride removal in an attempt to isolate the elements responsible for the rise in pH (Fig. 3, dashed lines). In this scenario, there is little change in pH$_C$ confirming that AE2 is responsible for alkalinization in our model. From the outset of the experiment, cytoplasmic Cl⁻ accumulates due to AE2 (Fig. 3B). The increased concentration changes the reversal potential causing Cl⁻ to leak back out through channels, which is electrogenic. Thus, prior to Cl⁻ removal from the outside, and after restoration of external Cl⁻, the membrane potential undergoes a slow depolarization (Fig. 3C).

3.2. Recovery of the cytoplasmic pH after an acid load

Cells are capable of preventing over acidification as well as alkalinization, and the Grinstein lab explored the mechanisms involved in recovery from an acid load in rabbit osteoclasts [29]. Isolated cells were incubated in 40 mM NH₄Cl and then rapidly transferred to NH₄⁺-free medium causing an efflux of neutral NH₃ from the cytoplasm and a concomitant rise in H⁺. When the transfer medium contained high Na⁺, the cytoplasm acidified down to pH 6.5 after 2 min followed by a slower recovery to pH 7.2 over the next 8 min (Fig. 4A, blue circles). When the external solution also contained high levels of amiloride (1 mM), a potent blocker of NHE antiporters, the cytoplasmic acidification was more profound followed by very weak recovery (Fig. 4A, solid black circles). We fit our model to these two situations simultaneously with all NHE active (red curve) or with no NHE (yellow dashed curve) mimicking the complete inhibition of NHE transporters by amiloride. The initial acidification of the cytoplasm was modeled as described in the *Theory and methods*, and the load concentration is identical in both calculations. Once pH$_C$ drops below 7, NHE is activated (Fig. 2D), and proton export via NHE counters the acid load resulting in a minimum pH$_C$ of 6.4 just after 1 min followed by a monotonic return to 7.2 that closely matches the experiment. The fitting procedure predicts that 213,218 NHE transporters are present in the plasma membrane to produce this recovery. When NHE are completely removed from the model, the acidification dips below pH 6 and never recovers during the remaining 9 min. It was hypothesized that the weaker recovery was due to other putative sodium dependent transporters present in the osteoclast plasma membrane [29], which our model does not include; hence, our model fails to reproduce the slow recovery mode facilitated by non-NHE mechanisms.

Next, the Grinstein lab tested whether pH$_C$ recovery from an acid load required Na⁺ by transferring to Na⁺-free external media high in K⁺ (Fig. 4B, blue circles) or high in N-methyl-D-glucammonium (NMG⁺), a non-blocking, non-permeant cation (Fig. 4B, solid black circles) [29]. The cytoplasmic pH recovers in high K⁺ lacking Na⁺, but the pH becomes 0.3 units more acidic and the recovery only returns to 7.0 after 10 min, not 7.2, when compared to the high Na⁺ experiment in panel A. Repeating the experiment in NMG⁺, without external K⁺ or Na⁺, produces an acidic cytoplasm of 5.9 with no recovery. The model was again fit to both of these experiments simultaneously resulting in semi-quantitative agreement. In high K⁺, the model does not become as acidic as the experiments, but matches the recovery phase quite well (red curve). NHE does not play in role in the recovery, but rather the high external K⁺ depolarizes the plasma membrane above −20 mV causing a small percentage (~1%) of H$_V$1 voltage-gated proton channels to open (Fig. 4B, inset), which can be inferred from the open channel probability contours in Fig. 2C. As pH$_C$ increases toward the external pH value, the H$_V$1 facilitated H⁺ current declines, as can be seen in the inset, and pH$_C$ approaches 7. The model predicts that 226,478 H$_V$1 channels are present in the membrane to produce this result. Under normal cellular bicarbonate conditions, AE2 typically resists cytoplasmic alkalinization by exporting bicarbonate. Unexpectedly, upon acid loading the cytoplasm, bicarbonate is consumed, and AE2 imports more HCO₃⁻, which assists in alkalinization to restore normal cytoplasm pH values and bicarbonate levels in panel B. Lastly, when Na⁺ is replaced by NMG⁺ the membrane potential remains near the K⁺ reversal potential at −68 mV, H$_V$1 channels remain closed, and pH$_C$ cannot recover from the acid load (yellow dashed curve), exactly as observed experimentally (solid black circles).

3.3. Modeling acidification of an active osteoclast

The experiments modeled in Figs. 3 and 4 provide estimates of particular elements of the mathematical model related to ion movement at the plasma membrane and pH regulation in the cytoplasm. Using these parameters as a base, we now explore the acidification of the extracellular matrix by an active osteoclast. Based on our previous work [22,27,
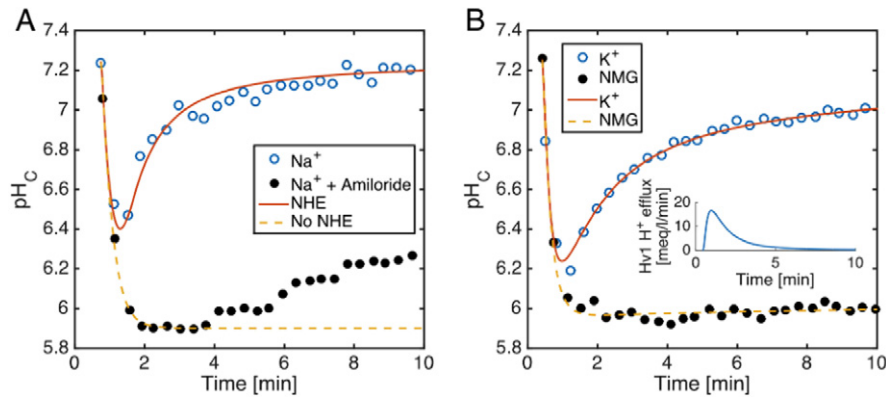
Fig. 4. Cytoplasmic pH recovery after an acid load. (A) Rabbit osteoclasts were acid loaded using NH$_4$Cl in 140 mM external Na$^+$ in the absence (blue circles) or presence (solid black circles) of 1 mM amiloride (all experimental data from Ref. [29]). The model was simultaneously fit to both data sets by varying N_{NHE}, and two parameters corresponding to the concentration of the cytoplasm NH$_4^+$ acid load and the removal rate of the external NH$_3$. The top curve was generated with 213,218 NHE transporters, which drive recovery by importing Na$^+$ and exporting H$^+$ (red curve). The amiloride data was fit by solving the model without NHE transporters (yellow dashed curve). (B) The experiments in panel A were repeated in 140 mM external K$^+$ (blue circles) or high external NMG$^+$ (solid black circles), both solutions lacking Na$^+$ (modeled here as 0.1 mM external Na$^+$). Again both data sets were simultaneously fit by varying N_{Hv1}, the passive potassium permeability across the plasma membrane (P_K), and acid loading parameters as before. The number of NHE antiporters was the value obtained in panel A. The model predicts that high K$^+$ depolarizes the cell opening H$_{V1}$ channels (226,478 channels) resulting in an efflux of protons (inset) and a recovery toward baseline cytoplasmic pH values (red curve). The non-permeant NMG$^+$ does not perturb the resting membrane potential, and no transport mechanisms are engaged to drive alkalinization (yellow dashed curve). We assumed that the currents due to Na$^+$/K$^+$-ATPase in both plots were negligible due to the low external Na$^+$.

32], we expect that the dynamics of acidification will be largely determined by the number of proton pumps and proton leak channels, spatial factors, and the buffering capacity of the released lysosomal contents and bone matrix, which is made up of hydroxyapatite and Type I collagen [64]. Unfortunately, there are only a handful of studies that have quantitated acidification values and rates to benchmark the model; however, it has been estimated that individual osteoclasts resorb bone at rates of 43–1225 μm^3/h [59], and Silver and co-workers used microelectrodes to measure the pH of the extracellular compartment formed by an active osteoclast tightly adhered to the plastic base of a petri dish (Fig. 5A, open blue circles) [63]. The probe was inserted into the extracellular compartment at time I and withdrawn when pH$_P$ went off scale at time W. This cell was able to acidify the ECC by 4 pH units in <4 min; however, not all cultured osteoclasts produced such a large drop in pH$_P$, in particular, those cells that failed to establish a tight seal to the substratum often produced only mildly acidic pits.

Using fixed parameters pertaining to the plasma membrane obtained earlier, we fit the model to the data by identifying optimal values for the ruffled border and ECC parameters listed in Table 2 such as ClC-7, V-ATPase, and H$_V$1 copy numbers as well as H$^+$ passive permeability (Fig. 1). We assume that K$^+$ leak channels have been excluded from this membrane, which we elaborate on in the Discussion. The fitting procedure was carried out between the two vertical, dashed red lines (the first corresponds to the probe insertion time). We terminated the fit prior to probe removal at W, since the V-ATPase profile used here cannot achieve such an acidic pH. We return to this issue in the Discussion. At time I we activated V-ATPases and ClC-7 antiporters mimicking the fusion of lysosomes with the ruffled border resulting in acidification of the pit. The best fit (Fig. 5A, purple dashed curve) only loosely matches the measured pH trace, and there are changes in the slope of the trace (particularly at 3 and 5 min) that are not captured by the model. Additionally, the final pH at 6 min is not as acidic as the experimental value. Silver and co-workers suggest that the cell settles during the acidification process causing changes to the ECC volume, which may be partially responsible for these slope changes. We assume that the geometric properties of the cell remained fixed during acidification, and we will explore geometric influences later.

The model predicts that the ruffled border has 528,286 active V-ATPases, 200,490 ClC-7 antiporters, and a passive proton permeability of 8.8 × 10^{-6} cm/s (Table 2). The initial fits to the data revealed that the model is sensitive to increases in passive proton permeability, but
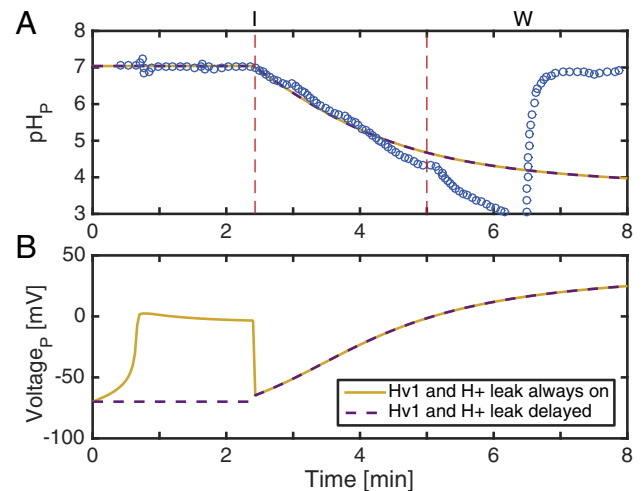

Fig. 5. Acidification of the extracellular compartment. (A) pH of the ECC of a single isolated osteoclast measured *in vitro* using a microelectrode (blue circles taken from Ref. [63]). Time I marks the time of insertion of the probe between the base of the petri dish and the cell, and W marks the time of withdrawal. All transporters and channels on the ruffled border were activated at time I. Predicted pH changes in the pit were determined by fitting the mathematical model to the experimental data between the two vertical red dashed lines (dashed purple curve). The fit was carried out over N_V and N_{ClC} resulting in 528,286 V-ATPases and 200,490 ClC-7. The passive proton permeability was set to 8.8 × 10^{-6} cm/s as discussed in the main text. A second calculation was carried out in which passive proton channels and H$_V$1 channels were present on the ruffled border prior to I at time 0 (yellow curve). Both calculations result in identical curves. (B) The membrane potential across the ruffled border for both calculations in panel A. In the absence of proton channel mediated currents, the membrane potential remains at the resting value of −71 mV prior to time I due to the electrical isolation of the ruffled border (dashed purple curve). Once acidification is initiated, the potential slowly climbs eventually becoming >0 mV due to Cl$^-$ efflux and H$^+$ entry via ClC-7. When proton currents are present on the ruffled border prior to proton pumping (yellow curve), the membrane potential depolarizes due to H$_V$1 channel opening, which allows proton entry into the cytoplasm. After proton pumping starts, the membrane potential hyperpolarizes due to fast proton efflux from the cytoplasm, and the subsequent time course for both scenarios is similar.

insensitive to decreases in permeability. Increasing the proton permeability to 6×10^{-6} cm/s, the value obtained from our earlier study of lysosomes [22], causes a 0.3 pH unit alkalinization of the pit and a noticeable decrease in the goodness of fit by ~12%. However, reducing P_H below 8.8×10^{-6} cm/s has no change on the solution, placing an upper limit on the proton permeability of the ruffled border.

The theoretical membrane potential across the ruffled border (Ψ_P) during acidification is shown in Fig. 5B. There are two curves corresponding to two different scenarios explored with the model (both of which give rise to indistinguishable pH_P traces in panel A). First, we assumed that H_V1 and intrinsic proton leak currents were delivered to the ruffled border with the other transporters at time I (purple dashed curve), and second, H_V1 and passive H^+ leaks were present in the ruffled border from time zero when the border is formed and becomes electrically isolated from the plasma membrane (yellow curve). The membrane potential starts at the resting plasma membrane potential of -71 mV at time 0, and in scenario 1, the lack of any currents prior to lysosomal fusion keeps the value constant. At time I, the membrane potential starts to rise due to the action of ClC-7 pumping Cl^- into the pit and removing H^+. H_V1 channels remain closed throughout, initially due to the negative membrane potential and later due to the acidic pH of the pit; therefore, in our model H_V1 does not aid in acidification of the pit. When H_V1 and the proton leak are present in the ruffled border from the start and K^+ channels are off or no longer present, Ψ_P starts to depolarize due to passive proton leak into the cytoplasm. Above -50 mV, a small fraction of H_V1 become active (still under 1%, see Fig. 2C) but enough to have a positive feed back causing greater depolarization and, therefore, a higher H_V1 open probability. The membrane potential quickly rises to the H^+ reversal at $+3$ mV, where the H_V1 open probability is 2–3%. The number of protons moved to change the potential from -70 mV to $+3$ mV is quite small so there is no detectable alkalinization of the pit (panel A). Once V-ATPase H^+ pumping starts, Ψ_P quickly hyperpolarizes due to V-ATPase mediated H^+ exit from the cytoplasm. Both scenarios then provide a similar time course of slow membrane depolarization. Please note that the degree of hyperpolarization in the second scenario at time I depends on the number of transport proteins, and the voltage does not return to the resting value in general.

3.4. ClC-7 versus a Cl^- channel

Next, we wanted to test the influence of ClC-7 on the acidification process. The Jentsch group discovered that loss of ClC-7 causes osteopetrosis [18], and osteoclasts lacking ClC-7 cannot form acidic compartments *in vitro* [21]. Moreover, a point mutation that converts the ClC-7 antiporter into a chloride *channel* results in more shallow resorption pits than osteoclasts with wild-type protein, and mice with the mutant antiporter exhibit a mild form of osteopetrosis [21]. We replotted the best fit to the pit acidification data in Fig. 5 with ClC-7 only (red curve), and then we refit the acidification curve with Cl^- channels only (purple dotted curve) (Fig. 6A). Finally, we carried out a calculation that included a mixture of both ClC-7 and Cl^- channels (yellow dashed curve). The time axis extends to 12 min to allow each system to reach steady state. As before, we did not model withdrawal of the probe. The rate of Cl^- counterion movement is a major determinant of the initial acidification rate, and channel and transporters are equally effective. However, the final steady state pH_P value that can be achieved in the pit is dependent on whether antiporters or channels are present in the ruffled border. As other modeling efforts have shown [21,22], ClC-7 alone provides the greatest degree of acidification to pH value of 3.6, a pure Cl^- channel results in the least acidification close to pH 5.0, and a linear combination of the two gives an intermediate pH_P value closer to the pure channel simulation. We previously argued that the downhill movement of H^+ from the acidic pit back into the cytoplasm energizes the Cl^- movement to more effectively reduce the membrane potential opposing proton pumping by the V-ATPase [22], which explains the current results.
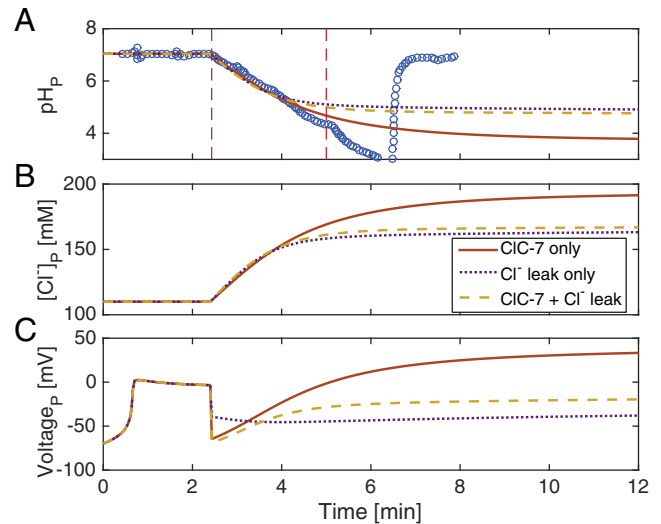

Fig. 6. ClC-7 aids acidification of the extracellular compartment. (A) ECC pH, (B) ECC chloride concentration, and (C) membrane potential of the ruffled border during pit acidification. Experimental values (blue circles) and values produced from a ClC-7 only model (red curve) are replotted from Fig. 5. A model with only Cl^- channels in the ruffled border, not ClC-7, was fit to the pH_P data between the vertical red lines in panel A (dotted purple curve) resulting in a less acidic pit. A mixed model with both ClC-7 and Cl^- channels (60% of the N_{ClC} plus 5% of P_{Cl}) produces an intermediate steady state pH_P value closer to the channel only result. For each scenario, the final $[Cl^-]_P$ concentration in panel B correlates with the degree of membrane depolarization in panel C.

Fig. 6B and C show the predicted chloride concentrations in the ECC and the membrane potential across the ruffled border, respectively, for each scenario using the same identification scheme as panel A. Chloride in the ECC starts at the extracellular value of 110 mM for all three cases, and during acidification the levels rise since the Cl^- serves as a counterion to offset the charge imbalance due to proton pumping into the pit. We predict that a pure channel will result in a final $[Cl^-]_P$ near 165 mM while ClC-7 antipoters alone produce a final value near 190 mM. The steady state Ψ_P correlate with the $[Cl^-]_P$ values – the larger the final pit chloride concentration, the larger the membrane potential, which in turn allows for greater acidification. Thus, ClC-7 alone achieves the greatest acidification due to the ability to bring more Cl^- into the pit.

3.5. AE2 influence on acidification

Chloride is a crucial counterion required to suppress the buildup of the membrane potential across the ruffled border during resorption, and bicarbonate export from the cytoplasm results in the creation of protons in the cytoplasm required by the V-ATPase for acidifying the ECC. To understand the role that AE2 exchangers on the plasma membrane play in pit acidification, we started from the base model parameters developed from the fits in Figs. 3–5 and then ran the model out to 1 h to determine the osteoclast conditions for a wide range of N_{AE} values ranging from 1000 to 10,000,000 exchangers. The cytoplasmic pH and Cl^- concentrations are independent of N_{AE} for values above 200,000, but pH_C climbs to 7.2 for low N_{AE} values and the cytoplasmic Cl^- concentration falls to near zero (Fig. 7A,C). Consequently, the chloride concentration in the pit drops for small AE2 numbers due to decreased $[Cl^-]_C$ (Fig. 7D). In other words, the reduced driving force for chloride entry into the pit makes it harder for ClC-7 to maintain high ECC chloride levels. The primary consequence of decreased $[Cl^-]_P$ is that the membrane potential across the ruffled border (Ψ_P) becomes less positive reducing the driving force for H^+ accumulation in the pit (Fig. 7E). Thus, the reduced membrane potential stalls the V-ATPase earlier and causes the pit to alkalinize by nearly 1 pH unit (Fig. 7B).
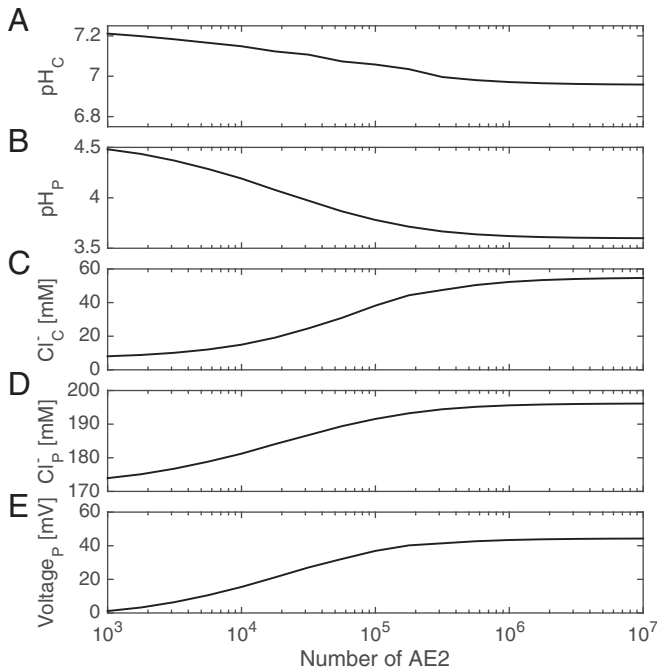
Fig. 7. Plasma membrane AE2 aids acidification of the extracellular compartment. The steady state values for (A) pH$_C$, (B) pH$_P$, (C) [Cl$^-$]$_C$, (D) [Cl$^-$]$_P$, and (E) Ψ_P over a wide range of AE2 transporters on the plasma membrane. Acidification of the pit was initiated as in Fig. 5 using the same values for all other parameters. For comparison, N_{AE} was 337,974 in Figs. 3 and 5.

3.6. Impact of pit volume and ruffled border size on the dynamics and steady state pH of the ECC

The geometry of a resorbing osteoclast is dynamic and difficult to quantify. The volumes and surface areas used throughout this study are estimated based on a few EM images, but these images are static and inherently low resolution. To better understand the role that membrane surface area and ECC volume have on the timecourse of acidification, we started with the model parameters from the acidification profile in Fig. 5 and scanned a wide range of ECC volumes and ruffled border surface areas, solving the time dependent equations for each set of values. We then plotted the pH value for each configuration at 15, 30, and 60 min in Fig. 8 (panels A-C, respectively). The transporter densities were held constant as surface area was changed, and the channel permeabilities were also held constant. The star in each panel indicates the surface area and volume in Fig. 5, and the grey regions along

the x-axis and y-axis are estimates of excluded geometries. Along the x-axis, the non-physical region corresponds to ECC volumes that are too large to be encompassed by the corresponding surface area, assuming a half-sphere model in which the ruffled border covers the upper half-sphere and the bone surface makes up the lower half. Along the y-axis, we assume that there is a finite space between the bone surface and the ruffled border, such that the pit volume must grow as the ruffled border grows. First, at steady state (well beyond 60 min) the pit pH approaches 3.7 for all surface areas and volumes. Hence, the capacitive change in the total membrane due to surface area changes is not an important determinant of pit pH. Moreover, the cytoplasm does not become emptied of protons even for very large pits. However, the time required to acidify is drastically different for different geometries. Small volumes (<200 μm³) and large surface areas (>500 μm²) reach steady state within 15 min, while large volumes (>800 μm³) and small surface areas (<500 μm²) require more than an hour to reach steady state. Thus, if the speed of bone break down is a limiting factor, it may explain why osteoclasts have such large ruffled borders and why the membrane fills the cavity as resorption occurs to minimize the ECC volume.

4. Discussion

Silver and co-workers observed acidification of the ECC below pH 3 (lower than the threshold of the probe) [63]; however, the mathematical model is only able to acidify the pit to 3.75 (see Fig. 5A). It is interesting to consider the theoretical maximum pH gradient that the V-ATPase can achieve in the absence of a membrane potential:

$$\Delta G = 23\, k_B T \cdot \frac{3\, \text{ATP}}{10\, \text{H}^+} = k_B T \ln\left(\frac{[\text{H}^+]_P}{[\text{H}^+]_C}\right) \Rightarrow \text{pH}_P = 4.0,$$

where [H$^+$]$_C$ is 10^{-7}, and ΔG is the free energy available per transported proton. We assume that the hydrolysis energy of a single ATP is 57 kJ/mol (23 $k_B T$) and that the stoichiometry of the V-ATPase is 3 ATP to 10 H$^+$ [44]. This theoretical maximum is 3 pH units, and Silver and colleagues indicated that isolated osteoclasts often produced pits 3 pH units lower the culture medium of pH 7, but sometimes they produce a gradient of 4 pH units [63]. In our model, pH$_C$ is ~7.0, indicating that the maximum pH$_P$ attainable is 4.0, and the model acidifies the pit 0.25 pH lower to 3.75 (Fig. 5A). As shown in Fig. 5B, the membrane potential across the ruffled border becomes positive during acidification due to counterion movement (Fig. 6C), and the electrical component of the PMF aids in dropping the pH lower than 4.0. Nonetheless, our model is unable to achieve the observed pH of 3 (Fig. 5A). Thus, we predict that the membrane potential across the ruffled border is close to 0 mV, or more likely, that it is positive, which is needed to explain
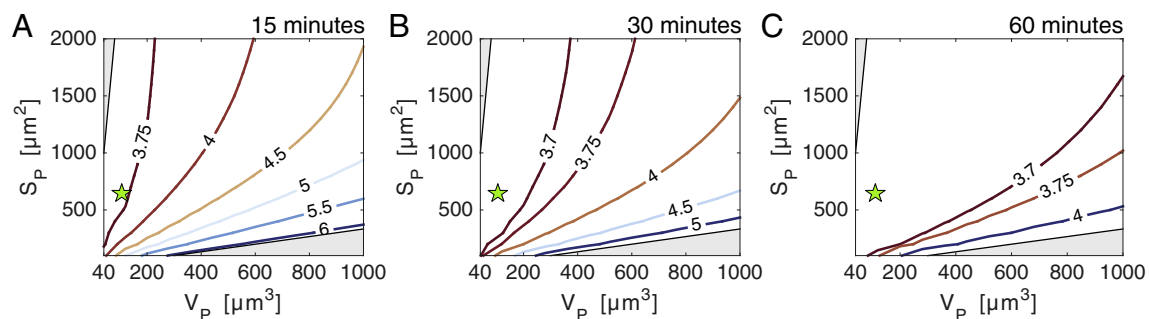

Fig. 8. The geometry of the ruffled border and extracellular compartment influence the kinetics of acidification. The pH of the pit at 15 min (A), 30 min (B), and 1 h (C) after initiation of acidification plotted as a function of the surface area of the ruffled border and volume of the ECC. All parameters are the same as those used in Fig. 5, except pump densities on the ruffled border were held constant for all simulations rather than total pump numbers. Green stars in each panel indicate default volume and surface areas used throughout the manuscript. Grey regions along the x-axis and the y-axis are estimates of unphysical regimes that delineate approximate bounds on the surface area and volume.

these extreme pH gradients. The model suggests that modulation of the membrane potential through one of the many elements in Fig. 1 may result in less acidic pits by hindering the proton pumping ability of the V-ATPase. Such pharmacological agents may provide a means of intervention for bone diseases resulting from over active osteoclasts.

Chloride plays an important role as a counterion during the acidification of organelles by creating a favorable environment for proton pumping [26,65], and mammals with mutations in the ClC-7 Cl^-/H^+ antiporter suffer from osteopetrosis [18] and their osteoclasts create shallower resorption pits [21]. Here we reproduce in Fig. 6 the results from a simpler model that first showed that ClC-7 aids acidification of the pit more than Cl^- channels [21]. We predict that the steady state Cl^- concentration in the ECC is quite high for ruffled borders containing only ClC-7 (~200 mM) and about 50 mM lower for Cl^- channels alone or mixtures of ClC-7 and Cl^- channels (Fig. 6B). The higher Cl^- concentrations in the ECC produced by ClC-7 result in a positive membrane potential while both the pure Cl^- channel and the mixed antiporter/channel models both result in negative membrane potentials between −40 and −25 mV, consistent with previous modeling efforts [21]. Coupling Cl^- flux to the downhill movement of protons out of the acidic pit enables ClC-7 to create a larger Cl^- gradient, as we highlighted in our earlier lysosome study [22], achieving a more favorable membrane potential for proton pumping by the V-ATPase (Fig. 6C). The chloride concentration in the cytoplasm also determines how much Cl^- is available for transport into the pit as well as the driving force for accumulation. Cytoplasmic Cl^- is controlled by the number of AE2 chloride-bicarbonate exchangers on the plasma membrane, and it is therefore not surprising that mutations in AE2 result in bone disease [37]. When AE2 numbers fall below 200,000, the cytoplasm cannot maintain nominal $[Cl^-]_C$ levels causing a drop in $[Cl^-]_P$, a rise in Ψ_P and a failure of the pit to fully acidify (Fig. 7). Thus, the model predicts that chloride handling at the plasma membrane and the ruffled border are both important for achieving low pH levels in the ECC. We want to note that the amount of Cl^- that accumulates in the pit at steady state is directly related to proton buffering capacity – higher buffering values produce higher Cl^- levels. We used a set of buffers with an effective constant buffering capacity of 25 mM/pH unit, and if the value increased to 40 mM/pH unit, for instance, we would predict ~50 mM more Cl^- than the values reported.

Our modeling efforts show that the presence of H_V1 channels in the plasma membrane can explain recovery of cytoplasmic pH after an acid load if the membrane potential has been depolarized (Fig. 4B). Current clamp experiments carried out on isolated rat osteoclasts indicate that the membrane potential adopts two stable values: −71 mV, close to the K^+ reversal potential, and −16 mV [66]. A bimodal behavior in the membrane potential has also been noted elsewhere [24,67]. Based on these bistable voltages, Nordstrom and co-workers suggested that an initial drop in Ψ_P to −16 mV may partially open H_V1 channels and allow protons to enter the ECC during the initial stages of resorption, but as the pit acidifies H_V1 would close preventing back flow [9,29]. Their hypothesis is based on a similar notion developed for the role that H_V1 may play in the early stages of the respiratory burst in neutrophils [68]. However, our calculations indicate that H_V1 opening does not acidify the pit, and if anything, protons leave the pit (Fig. 5A). That said, several groups have shown that Zn^{2+}, a potent inhibitor of H_V1, hinders bone resorption by osteoclasts [30], enhances bone formation in tissue culture [69], and also influences the course of osteoporosis [70]. While it is compelling to imagine that Zn^{2+} reduces bone breakdown by blocking H_V1 and preventing proton movement into the pit, we hypothesize that H_V1 channels influence osteoclast function by tuning the membrane potential. In the scenario where H_V1 and proton leak channels localize to the ruffled border and K^+ channels are turned off, the membrane depolarizes to ~0 mV prior to acidification (yellow curve in Fig. 5B). Depolarization of the membrane, aided by H_V1, may result in a transient rise in cytoplasmic calcium (Ca^{2+}) in the first few minutes that triggers lysosomal fusion to the ruffled border, which is required

for osteoclast function. Indeed, it is known that the exocytosis of lysosomes is Ca^{2+} mediated [71], and the lysosomal cation channel mucolipin 1 has been implicated in release in non-resorbing cells [72]. Moreover, Ca^{2+} 'puffs' have been observed in osteoclasts [73], and such brief bursts were previously suggested to play a role in maintenance of the ruffled border [12]. We speculate that in resorbing osteoclasts, once the ruffled border has become electrically isolated from the rest of the cell, H_V1 activation may depolarize the ruffled border causing a short, localized Ca^{2+} spike that initiates lysosomal fusion with the membrane. However, we note that prolonged increase in cytoplasmic Ca^{2+}, through the plasma membrane ryanodine receptor, results in osteoclast detachment and a decrease in resorption [74]. For this reason, the short depolarization in Fig. 5B followed by fast repolarization as acidification starts may be important for suppressing Ca^{2+} levels to promote resorption.

As mentioned earlier, ClC-7 alone produces the greatest level of acidification. If K^+ channels remain open in the ruffled border, the final pH of the ECC in Fig. 5A is 1 pH less acidic (not shown). Alkalnization occurs because the extracellular space, and hence the nascent ECC, has very little potassium (~5 mM), and K^+ flows into the pit where it builds up a positive charge. Additionally, K^+ channels suppress the depolarization of Ψ_P that occurs in the first 2 min prior to proton pumping, keeping the voltage clamped at −71 mV. Interestingly, if the ruffled border retains a small Cl^- leak channel (10^{-7} cm/s), in addition to H_V1, then Ψ_P depolarizes to −16.5 mV prior to proton pumping, consistent with the value of −17 mV observed electrophysiologically [66]. Unfortunately, the membrane potential of the ruffled border has not been quantitatively measured during acidification.

Mutations in the CAII gene are associated with bone disease [36], and Carano and co-workers have shown that the source for H^+-dependent acidification is CO_2 via CAII and Cl^--bicarbonate exchange [75]. Ideally we would have used the model to determine if the rate of H^+ and HCO_3^- production by CAII influences the pH of the pit. We expect that reducing the CAII rate, mimicking mutations to the CAII gene that render it less effective, will reduce the number of protons liberated in the cytoplasm during acidification of the pit. As the number of protons in the cytoplasm becomes depleted, it will become more difficult to acidify the pit due to both kinetic and thermodynamic factors. While this scenario is plausible, it will require quantitative modeling to determine if it correctly describes the underlying biological process.

The model presented here does not include components that likely affect osteoclast function. For instance, we did not include calcium, which is found in high concentration in deposited bone, and bone degradation liberates large amounts of Ca^{2+}. However, the in vitro experiments modeled in Figs. 5 and 6 were carried out on plastic petri dishes potentially mitigating the absence of Ca^{2+} from the model. Nonetheless, future modeling efforts will focus on the role of Ca^{2+} buffering, Ca^{2+} endocytosis, Ca^{2+} membrane fluxes, and potential roles that this ion may have on controlling aspects of resorption through Ca^{2+} receptors and changes in cytoplasmic calcium [76]. Vesicular transport of ECC material from the ruffled border to the plasma membrane is also an important feature of bone break down, which requires additional attention [77]. We also treated the buffering power of the ECC in a relatively simple manner assuming that it is a series of buffers characterized by a constant buffering capacity similar to values measured for lysosomes (Table 1). The ECC is composed of dissolved bone and lysosomal internal contents each of which has a complex makeup of polymer, protein, metabolites and ions. Future efforts will treat these substances with greater chemical accuracy based on known properties from the literature. We also treated the Na^+ and K^+ currents generated by the Na^+/K^+-ATPase in a very simple manner by assuming a constant flux over time. If we include a more realistic model of the ATPase from the literature, it will allow us to better understand the regulatory feedback that may exist between the Na^+ dependent NHE transporter and membrane voltage, which are set by cytoplasmic K^+ levels. Finally, as the ionic concentration of the ECC changes during

acidification, the active osmolyte content will also change creating a driving potential for water movement. We modeled the influence of geometry on the speed of acidification in Fig. 8, but the geometries were constant throughout each simulation. A more satisfying approach would be to model the physical and chemical forces driving geometry changes in the pit to better understand how, and if, acidification is coupled to shape.

5. Conclusion

We have assembled a comprehensive list of biophysical parameters from the literature that describe the conditions related to actively resorbing osteoclasts including the extracellular environment, cytoplasm, and extracellular compartment including relevant ion concentrations, geometric factors, buffering powers, and reaction rates (see Tables 1 and 2). These values are needed to construct a quantitative model of resorption, and they form a basis from which future modifications to the model can be made. The model does a good job at semi-quantitatively describing experiments involving pH changes in the cytoplasm and the extracellular compartment, and the model makes important hypotheses regarding variables that cannot be easily measured in experiment such as pump and channel numbers, membrane potential, and ionic concentration changes in time. Thus, our model has sufficient chemical detail to predict how changes in experimental setup, such as external ion concentrations, genetic mutations, and knockouts, will influence experimental results; and therefore, it can be used to drive new experiments. That said, we acknowledge that there are many elements of the model that are poorly characterized, which can limit the reliability of the results. For instance, cell geometry is difficult to estimate, and we have assumed a few constant values for many of the calculations presented here. If volume or surface areas are different from what we have assumed, the estimated pump numbers will be directly affected. Additionally, the pump numbers reported here directly depend on the single protein turnover rates shown in Fig. 2. If these rates are over or underestimated, the reported copy numbers will change. Finally, we have provided our source code for researchers to freely download and modify so that they can tailor components to their experimental system and use the solutions as a tool to help interpret their results (https://bitbucket.org/grabe-lab/). Currently, the code is in Matlab™, and requires access to this software to run; however, in the near future, a free version in python or Julia will be provided as well.

Acknowledgements

References

[1] W.J. Boyle, W.S. Simonet, D.L. Lacey, Osteoclast differentiation and activation, Nature 423 (6937) (2003) 337–342.

[2] A. Frattini, et al., Defects in TCIRG1 subunit of the vacuolar proton pump are responsible for a subset of human autosomal recessive osteopetrosis, Nat. Genet. 25 (3) (2000) 343–346.

[3] G.D. Roodman, Paget's disease of bone, Adv. Organ Biol. 5C (1998) 661–675.

[4] D.M. Black, et al., Randomised trial of effect of alendronate on risk of fracture in women with existing vertebral fractures. Fracture intervention trial research group, Lancet 348 (9041) (1996) 1535–1541.

[5] S.T. Harris, et al., Effects of risedronate treatment on vertebral and nonvertebral fractures in women with postmenopausal osteoporosis: a randomized controlled trial. Vertebral efficacy with Risedronate therapy (VERT) study group, JAMA 282 (14) (1999) 1344–1352.

[6] U.A. Liberman, et al., Effect of oral alendronate on bone mineral density and the incidence of fractures in postmenopausal osteoporosis. The alendronate phase III osteoporosis treatment study group, N. Engl. J. Med. 333 (22) (1995) 1437–1443.

[7] M.R. McClung, et al., Effect of risedronate on the risk of hip fracture in elderly women. Hip intervention program study group, N. Engl. J. Med. 344 (5) (2001) 333–340.

[8] B. Ettinger, et al., Reduction of vertebral fracture risk in postmenopausal women with osteoporosis treated with raloxifene: results from a 3-year randomized clinical trial. Multiple outcomes of Raloxifene evaluation (MORE) investigators, JAMA 282 (7) (1999) 637–645.

[9] A.V. Rousselle, D. Heymann, Osteoclastic acidification pathways during bone resorption, Bone 30 (4) (2002) 533–540.

[10] C. Supanchart, U. Kornak, Ion channels and transporters in osteoclasts, Arch. Biochem. Biophys. 473 (2) (2008) 161–165.

[11] F.H. Drake, et al., Cathepsin K, but not cathepsins B, L, or S, is abundantly expressed in human osteoclasts, J. Biol. Chem. 271 (21) (1996) 12511–12516.

[12] G. Stenbeck, Formation and function of the ruffled border in osteoclasts, Semin. Cell Dev. Biol. 13 (4) (2002) 285–292.

[13] H.C. Blair, et al., Osteoclastic bone resorption by a polarized vacuolar proton pump, Science 245 (4920) (1989) 855–857.

[14] S. Ohkuma, Y. Moriyama, T. Takano, Identification and characterization of a proton pump on lysosomes by fluorescein-isothiocyanate-dextran fluorescence, Proc. Natl. Acad. Sci. U. S. A. 79 (9) (1982) 2758–2762.

[15] T.H. Stevens, M. Forgac, Structure, function and regulation of the vacuolar (H+)-ATPase, Annu. Rev. Cell Dev. Biol. 13 (1997) 779–808.

[16] T. Michigami, et al., Novel mutations in the a3 subunit of vacuolar H(+)-adenosine triphosphatase in a Japanese patient with infantile malignant osteopetrosis, Bone 30 (2) (2002) 436–439.

[17] P. Dell'Antone, Evidence for an ATP-driven "proton pump" in rat liver lysosomes by basic dyes uptake, Biochem. Biophys. Res. Commun. 86 (1) (1979) 180–189.

[18] U. Kornak, et al., Loss of the ClC-7 chloride channel leads to osteopetrosis in mice and man, Cell 104 (2) (2001) 205–215.

[19] A.R. Graves, et al., The Cl−/H+ antiporter ClC-7 is the primary chloride permeation pathway in lysosomes, Nature 453 (7196) (2008) 788–792.

[20] B.E. Steinberg, et al., A cation counterflux supports lysosomal acidification, J. Cell Biol. 189 (7) (2010) 1171–1186.

[21] S. Weinert, et al., Lysosomal pathology and osteopetrosis upon loss of H + −driven lysosomal Cl- accumulation, Science 328 (5984) (2010) 1401–1403.

[22] Y. Ishida, et al., A model of lysosomal pH regulation, J. Gen. Physiol. 141 (6) (2013) 705–720.

[23] P.F. Lange, et al., ClC-7 requires Ostm1 as a beta-subunit to support bone resorption and lysosomal function, Nature 440 (7081) (2006) 220–223.

[24] J.H. Ravesloot, et al., Voltage-activated K+ conductances in freshly isolated embryonic chicken osteoclasts, Proc. Natl. Acad. Sci. U. S. A. 86 (17) (1989) 6821–6825.

[25] S.A. Arkett, S.J. Dixon, S.M. Sims, Substrate influences rat osteoclast morphology and expression of potassium conductances, J. Physiol. 458 (1992) 633–653.

[26] R.W. Van Dyke, Acidification of rat liver lysosomes: Quantitation and comparison with endosomes, Am. J. Phys. 265 (4 Pt 1) (1993) C901–C917.

[27] M.M. Wu, et al., Mechanisms of pH regulation in the regulated secretory pathway, J. Biol. Chem. 276 (35) (2001) 33027–33035.

[28] H. Sakai, et al., Increases in intracellular pH facilitate endocytosis and decrease availability of voltage-gated proton channels in osteoclasts and microglia, J. Physiol. 591 (Pt 23) (2013) 5851–5866.

[29] T. Nordstrom, et al., Regulation of cytoplasmic pH in osteoclasts. Contribution of proton pumps and a proton-selective conductance, J. Biol. Chem. 270 (5) (1995) 2203–2212.

[30] B.S. Moonga, D.W. Dempster, Zinc is a potent inhibitor of osteoclastic bone resorption in vitro, J. Bone Miner. Res. 10 (3) (1995) 453–457.

[31] D.M. Kallio, P.R. Garant, C. Minkin, Evidence of coated membranes in the ruffled border of the osteoclast, J. Ultrastruct. Res. 37 (1) (1971) 169–177.

[32] M. Grabe, G. Oster, Regulation of organelle acidity, J. Gen. Physiol. 117 (4) (2001) 329–344.

[33] P. Lehenkari, et al., Carbonic anhydrase II plays a major role in osteoclast differentiation and bone resorption by effecting the steady state intracellular pH and Ca2+, Exp. Cell Res. 242 (1) (1998) 128–137.

[34] T.J. Hall, T.J. Chambers, Optimal bone resorption by isolated rat osteoclasts requires chloride/bicarbonate exchange, Calcif. Tissue Int. 45 (6) (1989) 378–380.

[35] A. Teti, et al., Cytoplasmic pH regulation and chloride/bicarbonate exchange in avian osteoclasts, J. Clin. Invest. 83 (1) (1989) 227–233.

[36] W.S. Sly, et al., Carbonic anhydrase II deficiency identified as the primary defect in the autosomal recessive syndrome of osteopetrosis with renal tubular acidosis and cerebral calcification, Proc. Natl. Acad. Sci. U. S. A. 80 (9) (1983) 2752–2756.

[37] K. Josephsen, et al., Targeted disruption of the Cl−/HCO3– exchanger Ae2 results in osteopetrosis in mice, Proc. Natl. Acad. Sci. U. S. A. 106 (5) (2009) 1638–1641.

[38] Y. Moriyama, M. Maeda, M. Futai, Involvement of a non-proton pump factor (possibly Donnan-type equilibrium) in maintenance of an acidic pH in lysosomes, FEBS Lett. 302 (1) (1992) 18–20.

[39] T.J. Hall, T.J. Chambers, Na+/H+ antiporter is the primary proton transport system used by osteoclasts during bone resorption, J. Cell. Physiol. 142 (2) (1990) 420–424.

[40] J.H. Ravesloot, et al., Role of Na-H exchangers and vacuolar H+ pumps in intracellular pH regulation in neonatal rat osteoclasts, J. Gen. Physiol. 105 (2) (1995) 177–208.

[41] C.H. Leem, D. Lagadic-Gossmann, R.D. Vaughan-Jones, Characterization of intracellular pH regulation in the Guinea-pig ventricular myocyte, J. Physiol. 517 (Pt 1) (1999) 159–180.

[42] S.L. Rybak, F. Lanni, R.F. Murphy, Theoretical considerations on the role of membrane potential in the regulation of endosomal pH, Biophys. J. 73 (2) (1997) 674–687.

[43] M. Grabe, H. Wang, G. Oster, The mechanochemistry of V-ATPase proton pumps, Biophys. J. 78 (6) (2000) 2798–2813.

[44] J. Zhao, S. Benlekbir, J.L. Rubinstein, Electron cryomicroscopy observation of rotational states in a eukaryotic V-ATPase, Nature 521 (7551) (2015) 241–245.

[45] M. Walden, et al., Uncoupling and turnover in a Cl−/H+ exchange transporter, J. Gen. Physiol. 129 (4) (2007) 317–329.

[46] I.S. Ramsey, et al., A voltage-gated proton-selective channel lacking the pore domain, Nature 440 (7088) (2006) 1213–1216.

[47] M. Sasaki, M. Takagi, Y. Okamura, A voltage sensor-domain protein is a voltage-gated proton channel, Science 312 (5773) (2006) 589–592.

[48] V.V. Cherny, et al., Properties of single voltage-gated proton channels in human eosinophils estimated by noise analysis and by direct measurement, J. Gen. Physiol. 121 (6) (2003) 615–628.

[49] V.V. Cherny, V.S. Markin, T.E. DeCoursey, The voltage-activated hydrogen ion conductance in rat alveolar epithelial cells is determined by the pH gradient, J. Gen. Physiol. 105 (6) (1995) 861–896.

[50] R. Murphy, T.E. DeCoursey, Charge compensation during the phagocyte respiratory burst, Biochim. Biophys. Acta 1757 (8) (2006) 996–1011.

[51] F. Qiu, et al., Subunit interactions during cooperative opening of voltage-gated proton channels, Neuron 77 (2) (2013) 288–298.

[52] A. Gupta, J.C. Edwards, K.A. Hruska, Cellular distribution and regulation of NHE-1 isoform of the NA-H exchanger in the avian osteoclast, Bone 18 (2) (1996) 87–95.

[53] D. Taglicht, E. Padan, S. Schuldiner, Overproduction and purification of a functional Na+/H+ antiporter coded by nhaA (ant) from Escherichia coli, J. Biol. Chem. 266 (17) (1991) 11289–11294.

[54] B.D. Humphreys, et al., Functional characterization and regulation by pH of murine AE2 anion exchanger expressed in Xenopus oocytes, Am. J. Phys. 267 (5 Pt 1) (1994) C1295–C1307.

[55] R. Baron, et al., Evidence for a high and specific concentration of (Na+,K+)ATPase in the plasma membrane of the osteoclast, Cell 46 (2) (1986) 311–320.

[56] L.R. Pollack, E.H. Tate, J.S. Cook, Turnover and regulation of Na-K-ATPase in HeLa cells, Am. J. Phys. 241 (5) (1981) C173–C183.

[57] T. Akisaka, H. Yoshida, R. Suzuki, The ruffled border and attachment regions of the apposing membrane of resorbing osteoclasts as visualized from the cytoplasmic face of the membrane, J. Electron Microsc. 55 (2) (2006) 53–61.

[58] T. Arnett, Regulation of bone cell function by acid-base balance, Proc. Nutr. Soc. 62 (2) (2003) 511–520.

[59] J. Kanehisa, J.N. Heersche, Osteoclastic bone resorption: in vitro analysis of the rate of resorption and migration of individual osteoclasts, Bone 9 (2) (1988) 73–79.

[60] G. Schneider, et al., Three-dimensional cellular ultrastructure resolved by X-ray microscopy, Nat. Methods 7 (12) (2010) 985–987.

[61] W.F. Boron, Regulation of intracellular pH, Adv. Physiol. Educ. 28 (1–4) (2004) 160–179.

[62] W.H. Press, et al., Numerical Recipes Example Book (C), Cambridge University Press, New York, 1992 viii, 325.

[63] I.A. Silver, R.J. Murrills, D.J. Etherington, Microelectrode studies on the acid microenvironment beneath adherent macrophages and osteoclasts, Exp. Cell Res. 175 (2) (1988) 266–276.

[64] S.A. Nesbitt, M.A. Horton, Trafficking of matrix collagens through bone-resorbing osteoclasts, Science 276 (5310) (1997) 266–269.

[65] R.W. Van Dyke, J.D. Belcher, Acidification of three types of liver endocytic vesicles: similarities and differences, Am. J. Phys. 266 (1 Pt 1) (1994) C81–C94.

[66] S.M. Sims, S.J. Dixon, Inwardly rectifying K+ current in osteoclasts, Am. J. Phys. 256 (6 Pt 1) (1989) C1277–C1282.

[67] D.C. Mears, Effects of parathyroid hormone and thyrocalcitonin on the membrane potential of osteoclasts, Endocrinology 88 (4) (1971) 1021–1028.

[68] T.E. DeCoursey, V.V. Cherny, Potential, pH, and arachidonate gate hydrogen ion currents in human neutrophils, Biophys. J. 65 (4) (1993) 1590–1598.

[69] M. Yamaguchi, H. Oishi, Y. Suketa, Stimulatory effect of zinc on bone formation in tissue culture, Biochem. Pharmacol. 36 (22) (1987) 4007–4012.

[70] H. Fushimi, et al., Zinc deficiency exaggerates diabetic osteoporosis, Diabetes Res. Clin. Pract. 20 (3) (1993) 191–196.

[71] N.W. Andrews, Regulated secretion of conventional lysosomes, Trends Cell Biol. 10 (8) (2000) 316–321.

[72] D.L. Medina, et al., Transcriptional activation of lysosomal exocytosis promotes cellular clearance, Dev. Cell 21 (3) (2011) 421–430.

[73] W. Radding, et al., Intracellular calcium puffs in osteoclasts, Exp. Cell Res. 253 (2) (1999) 689–696.

[74] B.S. Moonga, et al., Ca(2+) influx through the osteoclastic plasma membrane ryanodine receptor, Am. J. Physiol. Renal. Physiol. 282 (5) (2002) F921–F932.

[75] A. Carano, et al., Acid and base effects on avian osteoclast activity, Am. J. Phys. 264 (3 Pt 1) (1993) C694–C701.

[76] M. Zaidi, et al., 'Calcium-activated' intracellular calcium elevation: a novel mechanism of osteoclast regulation, Biochem. Biophys. Res. Commun. 163 (3) (1989) 1461–1465.

[77] K. Mostov, Z. Werb, Journey across the osteoclast, Science 276 (5310) (1997) 219–220.

[78] B. Alberts, et al., Molecular Biology of the Cell, 5th ed. Garland Science, New York, 2008.

[79] A. Roos, W.F. Boron, Intracellular pH, Physiol. Rev. 61 (2) (1981) 296–434.

[80] M.M. Wu, et al., Organelle pH studies using targeted avidin and fluorescein-biotin, Chem. Biol. 7 (3) (2000) 197–209.

[81] N.D. Sonawane, J.R. Thiagarajah, A.S. Verkman, Chloride concentration in endosomes measured using a ratioable fluorescent Cl- indicator: evidence for chloride accumulation during acidification, J. Biol. Chem. 277 (7) (2002) 5506–5513.

[82] E.J. Crampin, N.P. Smith, A dynamic model of excitation-contraction coupling during acidosis in cardiac ventricular myocytes, Biophys. J. 90 (9) (2006) 3074–3090.

[83] B. Hille, Ion Channels of Excitable Membranes, 3rd ed. Mass.: Sinauer, Sunderland, 2001 (xviii, 814 p., [8] p. of plates).

[84] N.S. Krieger, N.E. Sessler, D.A. Bushinsky, Acidosis inhibits osteoblastic and stimulates osteoclastic activity in vitro, Am. J. Phys. 262 (3 Pt 2) (1992) F442–F448.